RSC Advances

ROYAL SOCIETY OF CHEMISTRY

www.rsc.org/advances

Cite this: DOI: 10.1039/c0xx00000x

www.rsc.org/xxxxxx

ARTICLE TYPE

Physicochemical characterization and catalytic CO oxidation performance of nanocrystalline Ce-Fe mixed oxides†

Putla Sudarsanam, Baithy Mallesham, D. Naga Durgasri, and Benjaram M. Reddy*

Received (in XXX, XXX) Xth XXXXXXXXX 20XX, Accepted Xth XXXXXXXXX 20XX

DOI: 10.1039/b000000x

ABSTRACT: The development of an efficient doped CeO_2 material is an active area of intense research in the environmental catalysis. In this study, we prepared highly promising Ce-Fe nano-oxides by a facile coprecipitation method and their catalytic performance was studied for CO oxidation. Various characterization techniques, namely, XRD, BET surface area, pore size distribution, Raman, FT-IR, TEM, H_2-TPR, and XPS were used to correlate the structure-activity properties of the Ce-Fe catalysts. XRD results confirmed the formation of nanocrystalline $Ce_{1-x}Fe_xO_{2-\delta}$ solid solution due to doping of Fe^{3+} into the CeO_2 lattice. The BET surface area and lattice strain of the CeO_2 are significantly improved after the Fe-incorporation. Raman studies revealed the presence of abundant oxygen vacancies in the Ce-Fe sample. TEM images evidenced the formation of nanosized particles with an average diameter of 5-20 nm in the prepared samples. Interestingly, despite the thermal treatment at higher temperatures, the Ce-Fe sample showed remarkable reducible nature compared to pure CeO_2 ascribed to existence of strong interaction between the CeO_2 and FeO_x. The synthesized Ce-Fe nano-oxides calcined at 773 K exhibited excellent CO oxidation performance (T_{50} = 480 K), with a huge difference of 131 K with respect to pure CeO_2 (T_{50} = 611 K). The outstanding activity of the Ce-Fe catalyst is mainly due to smaller crystallite size, facile reduction, enhanced lattice strain, and ample oxygen vacancies. The superior CO oxidation performance of Ce-Fe nano-oxides with the advantage of inexpensive and easy availability could make them as potential alternatives to noble metal-based oxidation catalysts.

1. Introduction

In recent years, the design of advanced doped ceria (CeO_2) materials is of great research interest due to their extensive use in several environmental and energy related catalytic applications.[1-4] The importance of doped CeO_2 has primarily derived from its remarkable oxygen storage/release capacity (OSC) and enhanced redox properties than pure CeO_2.[5-7] In addition, the incorporation of dopants into the CeO_2 results in the reduction of particle size to nanoscale range, hence more BET surface area.[6-9] Another potential advantage of doped CeO_2 is its strong resistance towards thermal sintering, and thereby, reasonable better catalytic performance even at higher temperatures.[5] Therefore, a large number of doped-CeO_2 oxides have been prepared by introduction of numerous transition and rare earth metal ions into the CeO_2 lattice.[1,10-12] However, the choice of a suitable dopant still remains a major challenge to the scientific community in terms of both activity and economical considerations.

Understanding the influence of various dopant features, such as oxidation state, ionic radius, dopant amount, redox nature, *etc*. on the structure-activity properties of the CeO_2 would provide valuable implications towards the selection of an appropriate dopant.[1,13,14] It has been shown that the substitution of Ce^{4+} by isovalent ions, like Zr^{4+} and Hf^{4+} enhance the OSC and redox properties of the CeO_2 and thus, improved CO oxidation activity.[15] Consequently, the Ce-Zr solid solutions have gradually replaced the pure CeO_2 as efficient OSC materials in three-way catalytic converters to reduce the automotive exhaust pollutants (CO, NO_x, and hydrocarbons).[16] Nonetheless, a considerable disadvantage associated with isovalent dopants is the difficulty of self-generation of oxygen vacancies through charge neutrality criterion.[17] Alternatively, the doping of aliovalent cations into the CeO_2 lattice is found to be a versatile way of modulating the CeO_2 characteristics.[18] For example, trivalent dopants (e.g., Gd^{3+} and Sm^{3+}) can promote the creation of large amount of extrinsic oxygen vacancies through charge compensation mechanism, along with intrinsic counterparts.[19]

It was reported that similarity of ionic radii between the host (Ce^{4+}) and guest ions (e.g., Eu^{3+} and Sm^{3+}) is essential for the development of promising doped CeO_2 catalysts.[5,20] In contrast, metal ions (e.g., Fe^{3+} = 0.68 and Mn^{3+} = 0.72 Å) having huge ionic radii disparity with respect to Ce^{4+} (0.97 Å) were also

Inorganic and Physical Chemistry Division, CSIR – Indian Institute of Chemical Technology, Uppal Road, Hyderabad – 500 607, India.
E-mail: bmreddy@iict.res.in; mreddyb@yahoo.com; Fax: +91 40 2716 0921; Tel.: +91 40 2719 1714.

†Electronic supplementary information (ESI) available: Pore size distribution, TEM, Williamson-Hall plots, XPS, and FT-IR profiles of Ce-Fe samples.

studied as plausible dopants.[10,21] On the other hand, the role of dopant amount was also considered in the modification of CeO_2 properties, indeed that strongly depends on the dopant nature.[22] For instance, the introduction of 50% Zr (balance with Ce) leads to superior lattice oxygen mobility and facile reduction of Ce^{4+} to Ce^{3+} compared to other dopant amounts, whereas 20% La-incorporation shows better structural and redox properties than 50% Zr-incorporation.[6,22] Interestingly, very small dopant amounts (≤ 10%) have also been employed for the preparation of smaller sized metal ion (Ni^{2+} and Co^{2+}) doped CeO_2 solid solutions.[23] Especially, it is indispensable to mention here that the redox character of the dopant could exhibit a favourable role in the improvement of the CeO_2 properties. It has been proved that the incorporation of tetravalent reducible dopants, such as Sn (Sn^{4+}/Sn^{2+}) and Ti (Ti^{4+}/Ti^{3+}) into the CeO_2 framework significantly enhances its catalytic activity (NO removal by CO) in comparison to non-reducible Zr-dopant.[13] Recently, Pintos *et al.*[24] reported that the trivalent metal ion, such as Mn^{3+} can be easily reduced to lower oxidation state by release of oxygen, which can significantly induces the oxygen storage and release capacity during CO-O_2 cycles. Zhang *et al.*[25] proposed a redox mechanism, in which, the lattice oxygen from the Fe_2O_3 participates in soot oxidation by the reduction of Fe^{3+} to Fe^{2+} and the resulting oxygen vacancies are refilled by lattice oxygen of CeO_2 through the reduction of Ce^{4+} to Ce^{3+}. Therefore, it can be expected that the reducible dopant not only improves the structure-activity properties of the ceria, but also participates itself in the catalytic reactions.

As one of the promising reducible dopants, Fe (Fe^{3+}/Fe^{2+}) has received much attention due to its unique beneficial properties.[21,26-29] Particularly, the redox potential of $Fe^{3+/2+}$ (0.77 V) is very much lower compared to $Ce^{4+/3+}$ (1.61 V).[26] As well, Fe is inexpensive, abundantly available, and environmentally harmless.[27] Hence, it can be believed that Fe-doped CeO_2 oxides may be able to solve the challenges of environmental catalysis that combines the promising reactivity with the economic cost-effective performance. To understand this, we prepared Ce-Fe nano-oxides by incorporation of 10 mol% Fe into the CeO_2 lattice by a facile coprecipitation method. The synthesized mixed oxides were calcined at different temperatures (773 and 1073 K) to explore their structural and textural stability. The catalytic efficiency of the Ce-Fe samples was studied for CO oxidation, a vital reaction in many industrial processes, such as automobile exhaust purification and CO preferential oxidation.[1] An extensive physicochemical characterization was undertaken by means of X-ray diffraction (XRD), transmission electron microscopy (TEM) and high resolution electron microscopy (HREM), Brunauer-Emmett-Teller (BET) surface area, Barrett-Joyner-Halenda (BJH) pore size distribution, X-ray photoelectron spectroscopy (XPS), Raman spectroscopy, Fourier transform infrared spectroscopy (FT-IR), and H_2-temperature programmed reduction (TPR) techniques. Great efforts have been made to understand the structure-activity properties of the Ce-Fe catalysts. Also, the CO oxidation performance of the Ce-Fe nano-oxides was correlated with various non-reducible metal doped CeO_2 oxides prepared by same preparation method.

2. Experimental details

2.1. Catalysts preparation

A simple coprecipitation method was adopted to prepare the CeO_2-Fe_2O_3 mixed oxides (Ce/Fe = 9/1) from ultra-high dilute aqueous solutions. In a typical procedure, appropriate amounts of $Fe(NO_3)_3 \cdot 9H_2O$ (Aldrich, AR grade) and $Ce(NO_3)_3 \cdot 6H_2O$ (Aldrich, AR grade) were dissolved in double distilled water under mild stirring conditions until the formation of a clear solution. An aqueous NH_3 solution (2.5 w/w%) was added slowly (min. 2 h duration) to the above mixture solution until pH of the solution reached to ~8.5. The obtained precipitates were decanted, filtered off, and washed with distilled water multiple times to remove the weakly adhered ions on the sample surface followed by oven drying at 393 K for 12 h. The oven dried sample was crushed using an agate mortar and calcined at 773 K for 5 h in air at a heating rate of 5 K min^{-1}. Finally, some portion of the finished catalyst was further calcined at 1073 K for 5 h using the same heating ramp to examine the thermal stability of the CeO_2-Fe_2O_3 catalyst. Pure CeO_2 was also prepared for comparison purpose by adopting the same precipitation method. For convenience, the prepared samples namely, pure CeO_2 and CeO_2-Fe_2O_3 are referred to as C773, C1073 and CF773, CF1073, where 773 and 1073 represent calcination temperatures, respectively.

2.2. Catalysts characterization

The powder XRD patterns were recorded on a Rigaku diffractometer using Cu Kα radiation (0.1540 nm), and operated at 40 kV and 40 mA. The diffraction patterns were recorded in the 2θ range of 2-80° with a step size of 0.02° and a step time of 2.4 s. The average crystallite size of the samples was determined by means of Scherrer equation from line broadening and the lattice parameter was estimated by a standard cubic indexation method using the intensity of the most prominent peak (111).

The BET surface area, pore volume, and pore size distribution measurements were performed using a Micromeritics ASAP 2020 instrument. Prior to analysis, the samples were degassed at 573 K for 3 h to remove any residual moisture. The BET surface areas were calculated from adsorption data in the relative pressure (P/Po) range = 0.04-0.25. Pore size and pore volume were calculated using the BJH method applied to the desorption leg of the isotherms. Williamson-Hall plots ($\beta\cos\theta/\lambda$ vs. $\sin\theta/\lambda$) were used to estimate the lattice strain of the catalysts. The TEM studies were carried out on a JEOL JEM-2100F instrument equipped with a slow-scan CCD camera, and the accelerating voltage of the electron beam was 200 kV. The preparation of samples for TEM analysis involved sonication in ethanol for 2-5 min followed by deposition on a copper grid. The FT-IR analysis was performed on a Nicolet 740 FT-IR spectrometer at ambient conditions using KBr discs with a nominal resolution of 4 cm^{-1} and averaging 100 spectra.

The vis-Raman analysis was carried out using a Horiba Jobin-Yvon HR800 Raman spectrometer equipped with a liquid-nitrogen cooled charge coupled device (CCD) detector and a confocal microscope. The emission line at 638-nm from Ar^+ laser (Spectra Physics) was focused on the sample under the

microscope with the diameter of the analyzed spot being ~1 μm. The acquisition time was adjusted according to the intensity of the Raman scattering. The wavenumber values reported from the spectra are accurate to within 2 cm^{-1}. The XPS measurements were carried out on a PHI 5400 instrument with a 200 W Mg-Kα probe beam. The analysis was done at room temperature and pressures were typically in the order of less than 10^{-8} Pa. The spectrometer was configured to operate at high resolution with a passing energy of 100 eV. Prior to the analysis, the samples were evacuated at high vacuum and then introduced into the analysis chamber. Survey and multi-region spectra were recorded at C 1s photoelectron peaks. Each spectral region of the photoelectron of interest was scanned several times to obtain good signal-to-noise ratios. Surface atomic ratios were calculated from peak area ratios normalized by the corresponding atomic sensitivity factors.

The H_2-TPR analysis was conducted using an automated catalyst characterization system (Micrometrics model AutoChem 2910) with a thermal conductivity detector (TCD). Approximately, 100 mg of sample was loaded in an isothermal zone of the reactor and heated at a rate of 10 K min^{-1} to 573 K in 30 mL min^{-1} He gas, which facilitates desorption of the physically adsorbed water. After the sample was cooled to room temperature, He was switched to 10% H_2/Ar with a rate of 20 mL min^{-1} and the temperature was linearly raised to 1073 K at a continuous heating ramp of 5 K min^{-1}, keeping all other parameters unchanged. The reactor effluent gas was passed through a molecular sieve trap to remove the produced water and was analyzed by gas chromatograph (GC) using the TCD, and the reduction of CuO to metallic copper was used for the calibration purpose.

2.3. Catalytic CO oxidation

The CO oxidation reaction was conducted in a fixed-bed microreactor under normal atmospheric pressure at 300-773 K using a heating rate of 5 K min^{-1}. Approximately, 125 mg catalyst sample (250–350 μm sieve fraction) was diluted with quartz particles of the same sieve fraction and was placed in a quartz reactor. The following gases and gas mixtures were used for pre-activation (10% O_2 in He) and CO conversion (1% CO, 0.5 or 1% O_2 in He) respectively. The samples were pre-activated at a rate of 5 K min^{-1} to 773 K using 10% O_2 in He gas at 60 mL min^{-1} flow rate. The total flow rates maintained by mass flow controllers were in the range of 180–190 mL min^{-1}. Analysis of the reactants and products was carried out using a GC equipped with TCD and connected to a personal computer (PC) for data acquisition. The CO (0–20000 ppm) and CO_2 (0–20000 ppm) gas concentrations were measured by IR spectrometer and the O_2 concentration was measured using a Magnos 16 analyzer (Hartmann & Braun). The CO/O_2 reactant feed ratio was 1 and the partial pressures of CO and O_2 were in the range of 10^3 Pa.

3. Results and discussion

The XRD patterns of pure CeO_2 and Ce-Fe samples calcined at different temperatures are shown in Fig. 1. It can be seen from Fig. 1 that the Ce-Fe sample calcined at 773 K exhibits the characteristic peaks related to the fluorite-structured CeO_2.[5,8,30] Surprisingly, very weak α-Fe_2O_3 peaks, along with CeO_2 peaks are also identified in the 1073 K calcined Ce-Fe sample, which might be due to Fe-segregation at elevated thermal treatments.[31] Interestingly, the XRD peaks of the CF773 sample are clearly shifted to higher angle side in comparison to pure CeO_2, whereas no considerable peak shift was noticed for the CF1073 sample (Fig. 1, inset). The observed peak shift in the CF773 sample is most probably due to difference in the ionic radii of host (Ce^{4+} ~0.97 Å) and guest (Fe^{3+} ~0.68 Å) ions.[6] The absence of XRD peaks related to Fe_2O_3 and shifting of CeO_2 peaks for the CF773 sample obviously reveal that Fe is completely incorporated into the CeO_2. To understand this, the lattice parameters of the Ce-Fe and pure CeO_2 samples were determined and the obtained values are presented in Table 1. It is evident from Table 1 that the CF773 sample exhibits decreased lattice parameter value (i.e., lattice contraction) in comparison to CeO_2 attributed to doping of smaller sized Fe^{3+} ions into the CeO_2 lattice. Conversely, no significant variations in the lattice parameter values were found between the pure CeO_2 and CF1073 sample, suggesting no incorporation of Fe into the CeO_2 matrix at higher calcination conditions. The estimated lattice parameters of the C773, C1073, CF773 and CF1073 samples are ~5.41, 5.41, 5.35, and 5.40 Å, respectively.

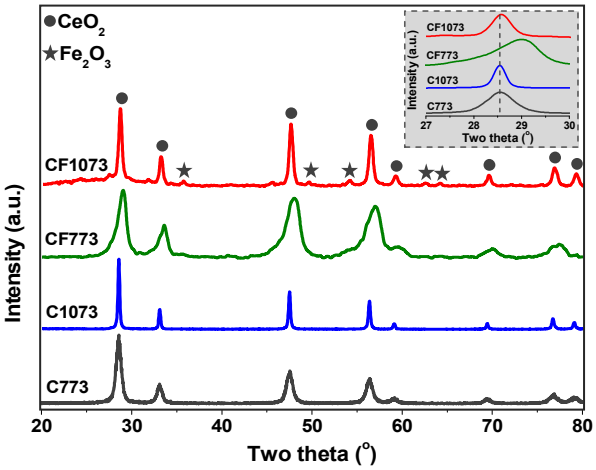

Fig. 1 Powder XRD patterns of pure CeO_2 (C) and CeO_2-Fe_2O_3 (CF) samples calcined at 773 and 1073 K.

Table 1 Average crystallite size (D), specific surface area (S), lattice parameter (LP), pore size (P), pore volume (V), and lattice strain (ε) of pure CeO_2 (C) and CeO_2-Fe_2O_3 (CF) samples calcined at 773 and 1073 K

Sample	D[a] (nm)	S (m^2/g)	LP[a] (Å)	P[b] (nm)	V[b] (cm^3/g)	ε[c]
C773	8.9	41	5.41	-	-	0.025
C1073	32.5	8	5.41	-	-	0.021
CF773	6.7	68	5.35	13.5	0.334	0.046
CF1073	19.9	15	5.40	38.2	0.055	0.028

[a] Estimated from XRD studies. [b] Determined from BJH analysis. [c] Calculated from Williamson-Hall plots.

Noticeably, the XRD peaks of the CF773 sample are very much broadened compared to other samples, which reveal the formation of smaller sized CeO_2 crystallites. The determined average crystallite sizes of the Ce-Fe and CeO_2 samples by means of Sherrer equation are shown in Table 1. The crystallite size of CeO_2 was significantly reduced after the Fe-incorporation, indicating the favourable role of Fe towards inhibition of the CeO_2 crystal growth. However, with the increase of calcination temperature from 773 to 1073 K, the crystallite size of Ce-Fe sample was drastically increased. The average crystallite sizes of C773, C1073, CF773 and CF1073 samples were found to be ~8.9, 32.5, 6.7 and 19.9 nm, respectively. The obtained specific surface area of the Ce-Fe and CeO_2 samples are summarized in Table 1. It was found that the introduction of Fe into the CeO_2 lattice considerably enhances its specific surface area from 41 to 68 m^2/g (Table 1). On the other hand, at elevated thermal treatments, the Ce-Fe sample exhibited very low specific surface area (15 m^2/g) that might be due to penetration of the segregated FeO_x species into the pores of the ceria. It is interesting to note from Table 1 that the Ce-Fe sample shows better textural properties (i.e., smaller crystallite size and higher specific surface area) compared to CeO_2 even at higher calcination temperatures. Generally, the decrease of particle size results in the improved surface area of the material.[32] Therefore, the higher specific surface area of the CF773 sample is most probably due to the presence of smaller sized CeO_2 crystallites (Table 1).

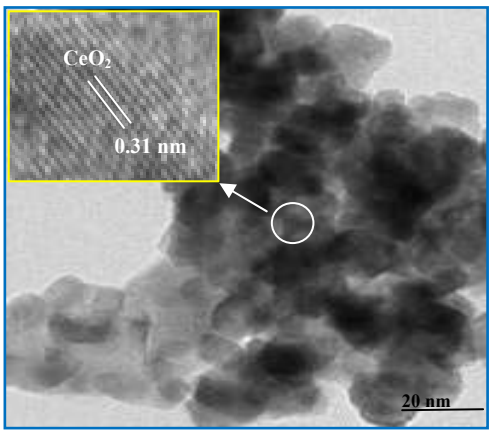

Fig. 2 HREM image of the CeO_2-Fe_2O_3 sample calcined at 773.

TEM and HREM analyses were performed to explore the structural evolution of the prepared samples at atomic scale. It must be mentioned here that the calculation of particle size from TEM images of the metal oxides and mixed metal oxides, especially for ceria-based materials, prepared by precipitation methods is rather difficult as no protective agents are used like in the present study. As stated, no precise estimation of the particle size from the obtained TEM pictures was attempted in the present study (Fig. S1, ESI†). However, all samples exhibited nanosized particles in the broad range of 5-20 nm. A meticulous examination of the TEM images revealed that the 1073 K calcined samples show slightly larger sized particles in comparison to 773 K calcined samples. On the other hand, the HREM analysis of the CF773 sample clearly shows the lattice fringes with the spacing of ~0.31 nm, which can be assigned to the CeO_2 (111) with the XRD peak at 28.6° (Fig. 1). The estimation of lattice strain provides useful information about the defective nature of the CeO_2-based materials.[33] It was reported that doping of lower-valent cations facilitates defect formation within the CeO_2 lattice by generating lattice strain, which eventually improves the extrinsic surface defects, resulting in superior CO oxidation performance.[34,35] Williamson-Hall method was employed to determine the lattice strain of the CeO_2 and Ce-Fe samples (Fig. S2, ESI†).[33] It was found that the CF773 sample exhibits highest lattice strain (Table 1), which might be one of the reasons for its superior CO oxidation performance as discussed in the activity part. Interestingly, a negligible variation in the lattice strain values of the CF1073 and C773 samples was noticed, suggesting that no Fe-incorporation into the CeO_2 lattice for the CF1073 sample, which is in consistent with the lattice parameter measurements (Table 1). Fig. 3 shows the N_2 adsorption-desorption isotherms of the Ce-Fe samples. The obtained isotherms can be classified as Type IV isotherms with H1-type hysteresis, which are characteristic of the mesoporous materials.[36] The determined data from the BJH model indicate narrow pore size distribution with an average pore diameter of 13.5 and 38.2 nm for the CF773 and CF1073 samples (Table 1), respectively (Fig. S3, ESI†). On the other hand, the CF773 sample shows larger pore volume (0.334 cm^3/g) than CF1073 sample (0.055 cm^3/g).

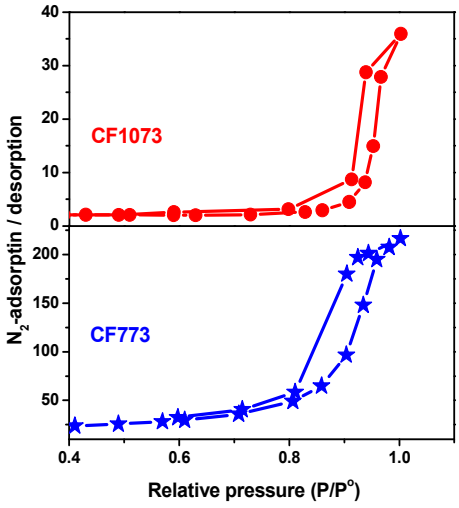

Fig. 3 N_2 adsorption-desorption isotherms of Ce-Fe (CF) catalysts calcined at 773 and 1073 K.

Raman spectroscopy was utilized to understand the structural properties of the Ce-Fe mixed oxides (Fig. 4). As can be seen from the Fig. 4, all samples show a prominent band at around 445-460 cm^{-1}, corresponding to the F_{2g} vibration of the cubic fluorite type CeO_2 that support the observations made from the XRD studies.[8] The F_{2g} band of Ce-Fe samples obviously shifted to lower wavenumbers with broadening compared to pure CeO_2, which is more pronounced in the case of CF773 sample. The noticed peak shift and its broadening depends on various parameters, including the crystal defects, oxygen vacancies, phonon confinement, and inhomogeneous strain related to the reduced ceria.[15,37] Generally, in trivalent metal doped CeO_2 two

types of oxygen vacancy bands are observed at around 545 and 600 cm^{-1} attributed to incorporation of trivalent metal ions into the CeO_2 lattice and the presence of Ce^{3+} ions, respectively.[8,9,19] It is well-known that the reduction of two adjacent Ce^{4+} ions to Ce^{3+} ions leads to generation of one oxygen vacancy in CeO_2.[38,39,40] On the other hand, the substitution of Ce^{4+} by Fe^{3+} results in the creation of an oxygen vacancy for every two Fe^{3+} dopants to balance the charge in the CeO_2 lattice.[9] From XPS studies (Fig. 5), it was clear that the Ce-Fe samples contain the Ce^{3+} ions, along with the Ce^{4+} ions. Therefore, the synthesized Ce-Fe samples are supposed to exhibit two types of oxygen vacancy bands due to Fe^{3+}-incorporation and the presence of Ce^{3+} ions. However, to our surprise, the CF773 sample showed only one oxygen vacancy band at ~600 cm^{-1} (Fig. 4, inset), corresponding to Ce^{3+} ion promoted oxygen vacancies. It has been reported that small doping amounts of Fe improve the oxygen vacancy concentration (vacancy compensation mechanism), whereas large amounts of Fe annihilate them (dopant interstitial compensation mechanism).[28] Li *et al.*[9] have showed that the oxygen vacancies generated due to the Fe^{3+}-incorporation can be compensated by the presence of interstitial Fe^{3+} even for smaller doping amounts of Fe (15%). Moreover, it must be understood here that the observation of Raman band with relatively low oxygen vacancy concentration is extremely difficult in the case of CeO_2-based oxides.[41] Therefore, it can be suggested that the absence of oxygen vacancy band at around 545 cm^{-1} in the CF773 sample might be either due to the existence of interstitial Fe^{3+} ions or negligible concentration of the oxygen vacancies. Previous works also reported only one oxygen vacancy band in the case of Ce-Fe mixed oxides.[25,42]

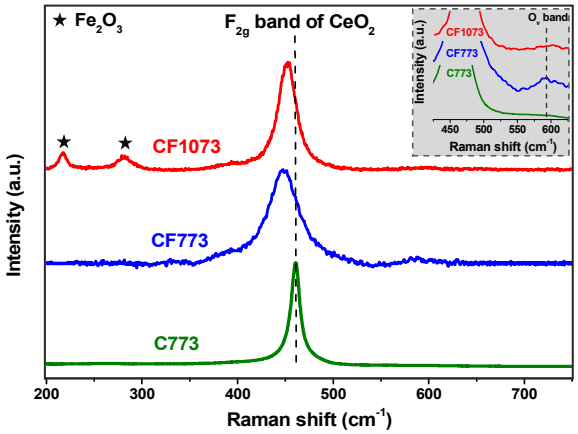

Fig. 4 Visible Raman spectra of pure CeO_2 (C773) and CeO_2-Fe_2O_3 (CF) samples calcined at 773 and 1073 K.

On the other hand, no oxygen vacancy band was found for the CF1073 sample. Usually, oxygen vacancies are generated due to release of loosely bound oxygen ions from the octahedral interstitial sites, which are formed due to relocation of the oxygen ions from the tetrahedral sites to the octahedral sites.[40] At higher temperatures (~1073 K), the oxygen ions can achieve sufficient energy to overcome the potential barrier to fill up the tetrahedral sites from the octahedral sites, which can hardly be removed from the lattice. As asserted, in the present work also, no visible oxygen vacancy band (Fig. 4, inset) was identified in the 1073 K calcined Ce-Fe sample. In addition to the F_{2g} band, the CF1073 sample exhibited two bands at ~216 and ~280 cm^{-1}, indicating the presence of α-Fe_2O_3 (hematite) phase with the D^6_{3d} crystal space group.[43] Interestingly, no α-Fe_2O_3 peaks were noticed in the CF773 sample, confirming the formation of CeO_2 solid solution, and corroborates the XRD results very well.

XPS analysis was undertaken to know the oxidation states of the elements present in the Ce-Fe samples as well as to understand the influence of the dopant (Fe) on the chemical environment of the cerium and oxygen. Fig. 5 shows the Ce 3d core level spectra of the CeO_2 (inset) and CeO_2-Fe_2O_3 samples. The obtained binding energies (BE) of the Ce $3d_{3/2}$ (u'''), Fe $2p_{3/2}$ and O 1s are summarized in Table 2. The Ce 3d XP spectrum of CeO_2-based materials is known to be complex due to the hybridization of Ce 4f with ligand orbitals and fractional occupancy of the valence 4f orbitals.[6,8] This unnecessary hybridization assists the multiplet splitting of the peaks into doublets, with each doublet showing further structure due to final state effects.[6] As shown in the Fig. 5, the curves of Ce 3d spectra are composed of ten peaks corresponding to five pairs of spin-orbit doublets. The peaks labelled 'v' indicates Ce $3d_{5/2}$ contributions and those of labelled 'u' represent the Ce $3d_{3/2}$ contributions. The dominant peaks denoted by v, v'', v''', u, u'' and u''' indicate the $3d^{10}4f^0$ state of Ce^{4+} ions, whereas those marked by v_0, v', u_0 and u' represent the $3d^{10}4f^1$ initial electronic state of the Ce^{3+} ions. Identification of these peaks reveals coexistence of Ce^{3+} and Ce^{4+} in all samples. Interestingly, the binding energy of the u''' peak was considerably decreased for the Ce-Fe samples with respect to the pure CeO_2 (Table 2), indicating the influence of the dopant on the chemical environment of the CeO_2.[10] This noteworthy result suggests the improved reducible nature of the CeO_2 in the Ce-Fe samples. Moreover, a meticulous observation of the Fig. 5 reveals that the intensity of the u''' peak (a qualitative fingerprint of Ce^{4+} ions) was increased with increase of calcination temperature, which signifies the presence of higher amount of Ce^{3+} ions in the CF773 sample compared to CF1073 sample.[5,6] However, it must be mentioned here that the conversion of Ce^{4+} to Ce^{3+} is also possible under ultra-high vacuum conditions during the XPS measurements.[44]

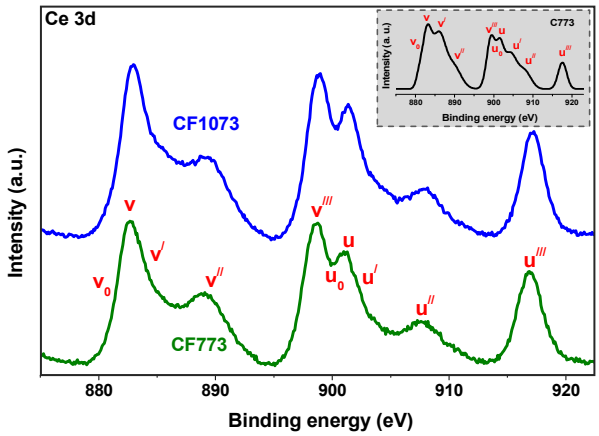

Fig. 5 Ce 3d XPS profiles of pure CeO_2 (C773, inset) and CeO_2-Fe_2O_3 (CF) samples calcined at 773 and 1073 K.

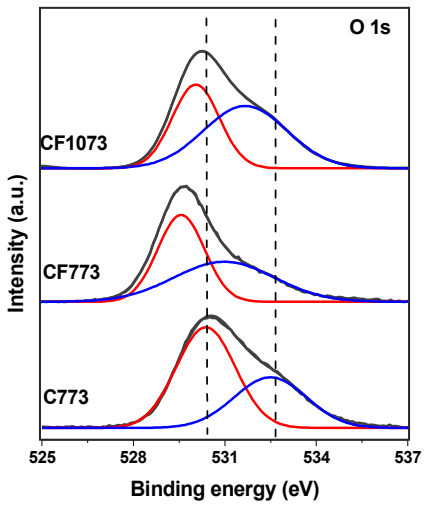

Fig. 6 O 1s XPS profiles of pure CeO_2 (C773) and CeO_2-Fe_2O_3 (CF) samples calcined at 773 and 1073 K.

The O 1s core-level spectra of CeO_2 and Ce-Fe samples are shown in Fig. 6. Clearly, the O 1s spectrum of all samples is composed of more than one type of oxygen ions.[22,45] The observed main peak at ~530.0±0.5 eV can be assigned to lattice oxygen of the CeO_2. Appearance of another peak at ~532.0±0.3 eV reveals the existence of various hydroxyl and/or carbonyl groups on the catalyst surface, which are further confirmed by FT-IR study (Fig. S4, ESI†). Generally, the surrounding environment of the lattice oxygen in trivalent (e.g., Sm^{3+} or Gd^{3+}) doped CeO_2 could be different from that of pure CeO_2 due to difference in the electronegativity of the dopant and cerium.[46] In the present work also, the chemical environment of lattice oxygen was significantly changed after the Fe incorporation (CF773 sample) evidenced by shifting of lattice oxygen peak towards lower binding energy (Table 2). As asserted, this fascinating observation can be explained by a huge electronegativity disparity of the dopant (Fe ~1.83) and Ce (1.12). Owing to lower binding energy, the lattice oxygen becomes more labile, which might be responsible for the generation of oxygen vacancies in the CF773 sample (Fig. 4). On the other hand, a negligible lattice oxygen peak shifting is observed in the case of CF1073 sample (Table 2), suggesting no influence of the Fe on the chemical environment of CeO_2 lattice oxygen. This unusual observation is certainly due to Fe segregation at higher calcination temperatures (evidence from XRD and Raman studies). The binding energies of Fe $2p_{3/2}$ and Fe $2p_{1/2}$ are identified at ~711.2 and ~724.2 eV, with two satellite peaks at ~718.7 and ~732.4 eV, respectively, confirming the presence of Fe^{3+} in the Ce-Fe samples (Fig. S5, ESI†).[25]

The surface Ce/Fe atomic ratios for all the samples are estimated from the XPS analyses of the Ce-Fe samples. If the Ce and Fe cations are randomly distributed throughout the sample, the expected Ce/Fe ratio must be = 9. However, the obtained Ce/Fe atomic ratio for the CF773 sample was ~9.356, which is strongly deviated from the expected value attributed to segregation of Ce ions at the surface and/or enrichment of Fe ions in the bulk. Interestingly, with the increase of calcination temperature from 773 to 1073 K, there is a considerable decrease in the Ce/Fe atomic ratio (~9.186), indicating the diffusion of Fe^{3+} ions to the catalyst surface. Therefore, there is a possibility for the segregation of Fe species at higher calcination temperatures, in agreement with the XRD and Raman studies of the CF1073 sample.

Table 2 XPS core level binding energies of Ce, O, and Fe for pure CeO_2 (C773) and Ce-Fe (CF) samples calcined at 773 and 1073 K

Sample	$Ce3d_{3/2}$ (u'''), eV[a]	O 1s, eV[b]	Fe $2p_{3/2}$, eV[c]
C773	917.5	530.3	–
CF773	916.8	529.5	711.2
CF1073	917.0	530.1	711.3

[a] From Ce 3d spectra. [b]From O 1s spectra. [c] From Fe 2p spectra

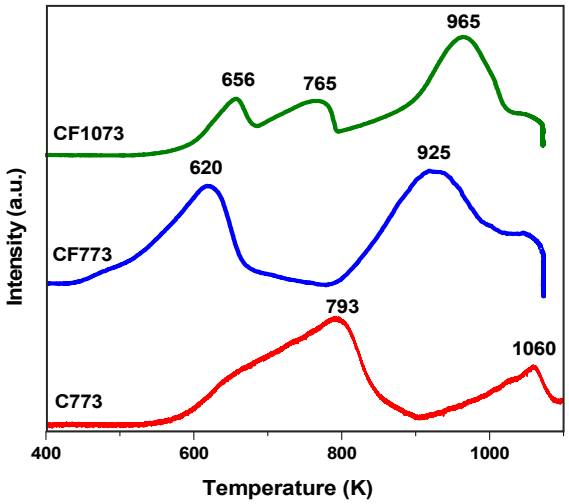

Fig. 7 H_2-TPR profiles of pure CeO_2 (C773) and CeO_2-Fe_2O_3 (CF) samples calcined at 773 and 1073 K.

Fig. 7 shows the H_2-TPR profiles of pure CeO_2 and Ce-Fe samples calcined at different temperatures. Usually, pure CeO_2 exhibits two reduction peaks at ~793 (low-temperature, LT) and ~1060 K (high-temperature, HT) due to reduction of surface-capping of oxygen and bulk-phase lattice oxygen, respectively.[44] Due to lower enthalpy of reduction, the outermost layers of the CeO_2 are first reduced at lower temperatures, followed by bulk reduction at higher temperatures.[47] It is a well-known fact in the literature that the incorporation of a metal ion into the ceria lattice significantly enhances its reducible nature. As stated, the CF773 sample showed very much lower reduction temperatures (i.e., ~620 and ~925 K) in comparison to pristine ceria attributed to doping of Fe^{3+} ions into the CeO_2 lattice. Interestingly, the CF1073 sample exhibited three reduction peaks at ~656, 765 and 965 K, of which two peaks can be assigned to surface and bulk reduction of the CeO_2 and the remaining peak might be due to the Fe_2O_3 species present in the CF1073 sample (evidence from XRD and Raman studies). Pristine Fe_2O_3 normally shows two step reduction, i.e., $Fe_2O_3 \rightarrow Fe_3O_4$ and $Fe_3O_4 \rightarrow Fe$ (0) at ~658 and

~863 K, respectively.[25,31,48] Therefore, by correlating the reduction temperatures of the Fe_2O_3 with that of CF1073 sample, the observed reduction peak at ~656 K in the CF1073 sample can be assigned to the $Fe_2O_3 \rightarrow Fe_3O_4$ transition. On the other hand, no reduction peak related to the Fe_2O_3 species was noticed in the CF773 sample that might be due to the absence of Fe_2O_3 species. Besides having the low specific surface area, the CF1073 catalyst showed better reducible nature than pure CeO_2. This interesting observation can be explained by the existence of strong interaction between the segregated Fe species and CeO_2.[49]

Table 3 Comparison of the structure-activity properties of pure CeO_2 (C773) and CeO_2-Fe_2O_3 (CF) samples calcined at 773 and 1073 K

Sample	BET surface area (m^2/g)	Reduction peaks[a]		Lattice strain[b]	T_{50} (K)[c]
		LT	HT		
C773	41	793	1060	0.025	611
CF773	68	620	925	0.046	480
CF1073	15	765	965	0.028	608

[a] Determined from H_2-TPR results (LT – low temperature and HT – high temperature). [b] Estimated from Williamson-Hall plots. [c] Obtained from CO oxidation activity results.

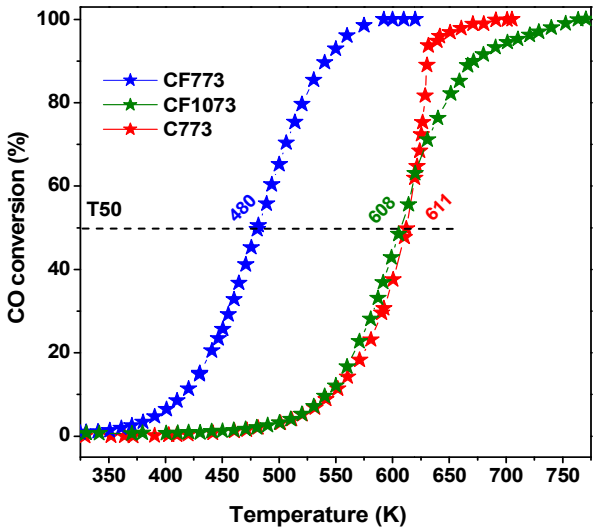

Fig. 8 Oxidation of CO over pure CeO_2 (C773) and CeO_2-Fe_2O_3 (CF) samples calcined at 773 and 1073 K.

The catalytic efficiency of the Ce-Fe samples was investigated for CO oxidation and the obtained results are shown in Fig. 8. It was found that the CO conversion increases with the increase of reaction temperature for all samples. The relative order of the catalyst activity can be evaluated by comparing the T_{50} values (T_{50} = temperature at which 50% CO conversion is achieved). Amongst, the CF773 sample exhibited remarkable CO oxidation performance at much lower temperature (T_{50} = 480 K), with a huge difference of 131 K in comparison to the pure ceria (T_{50} = 611 K). The enhanced lattice strain, facile reducible nature, ample oxygen vacancies, and improved BET surface area are found to be the decisive factors for high catalytic activity of the CF773 sample (Table 3). Despite its low surface area, the CF1073 sample showed comparable CO oxidation activity (T_{50} = 608 K) with that of CeO_2 (T_{50} = 611 K). Ma *et al.*[50] reported that FeO_x species present on the Pt surface provide sufficient active oxygen species for CO oxidation. As mentioned in the introduction part, the lattice oxygen of the Fe_2O_3 also participates in soot oxidation through facile reduction of Fe^{3+} to Fe^{2+} and the generated vacancy can be refilled by CeO_2 lattice oxygen.[25] Hence, it can be expected that the Fe_2O_3 species present on the surface of CF1073 sample provides adequate active oxygen species for CO oxidation. The formed oxygen vacancies can be refilled by migration of the oxygen from the CeO_2 lattice due to existence of strong interaction between CeO_2 and Fe_2O_3 species (evidence from H_2-TPR studies). Although no oxygen vacancies were found in the pure CeO_2, its catalytic activity could be attributed to facile generation of oxygen vacancies under reaction conditions, followed by rapid and repeatable redox cycles of Ce^{4+}/Ce^{3+}.[20]

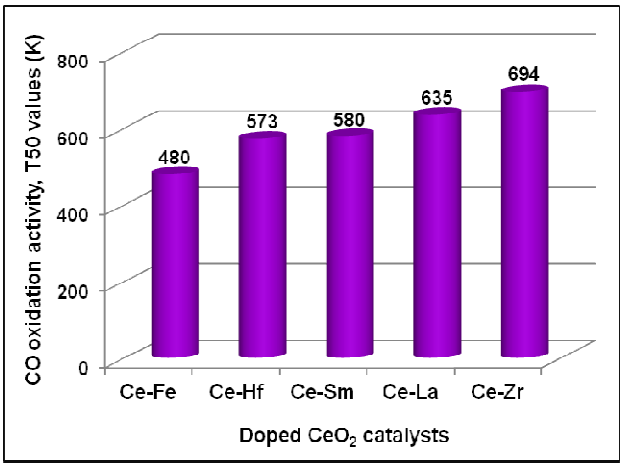

Fig. 9 Correlation of CO oxidation performance (T_{50} values) of Ce-Fe, Ce-Hf, Ce-Sm, Ce-La, and Ce-Zr mixed oxides.

Finally, we have made an attempt to correlate the performance (T_{50} values) of the Ce-Fe nano-oxides with that of Ce-Hf,[15] Ce-Sm,[5] Ce-La,[44] and Ce-Zr[15] catalysts prepared by same copreparation method (Fig. 9). It was found that the Ce-Fe sample exhibits 50% CO conversion at much lower temperatures compared to other doped CeO_2 samples. An interesting observation can be noted from Fig. 9 is that only Fe exhibits reducible nature, whereas Hf, Sm, La, and Zr are non-reducible dopants. Therefore, it can be suggested that the reducible nature of the dopant plays a beneficial role in the CO oxidation activity of the CeO_2. The superior CO oxidation activity of Ce-Fe nano-oxides is expected to bring new opportunities in the design of efficient CeO_2-based catalysts to replace the noble metal-based catalysts for industrially important oxidation reactions.

4. Conclusions

In this work, we developed highly economical Ce-Fe nano-oxides with excellent CO oxidation performance by a simple coprecipitation method using ultra-high dilute aqueous solutions. Characterization studies revealed the favourable role of Fe in the

enhancement of structural, textural, and redox properties of the CeO_2. However, at elevated thermal treatments, the crystallite size, specific surface area, and lattice strain of the Ce-Fe sample are adversely affected, which is attributed to Fe-segregation. TEM images showed the presence of nanosized particles with an average diameter of 5-20 nm in the prepared samples. Raman analysis indicated the existence of considerable amount of oxygen vacancies in the Ce-Fe sample. XPS studies revealed the influence of Fe on the chemical environment of the cerium and oxygen. H_2-TPR studies showed that the addition of Fe to the CeO_2 remarkably enhances its reducible nature by shifting the surface and bulk reduction to lower temperatures. The Ce-Fe sample calcined at 773 K exhibited superior CO oxidation activity at much lower temperatures (T_{50} = 480 K), due to its improved reducible nature, enhanced lattice strain, and ample oxygen vacancies. Despite its low surface area, the CF1073 sample showed comparable CO oxidation performance with that of pure CeO_2 attributed to existence of strong interaction between the CeO_2 and Fe_2O_3 species. The correlation of CO oxidation performance of Ce-Fe nano-oxides with various doped CeO_2 oxides revealed that the reducible nature of the dopant plays a favourable role in the improvement of catalytic efficiency of the CeO_2.

Acknowledgments

P. S., B. M., and D. N. thank the Council of Scientific and Industrial Research (CSIR), New Delhi for research fellowships. We also greatly thank Prof. W. Grünert, RUB, Germany, for providing CO oxidation results. Financial support was received from Department of Science and Technology, New Delhi, under SERB Scheme (SB/S1/PC-106/2012).

References

1 Y. Liu, C. Wen, Y. Guo, G. Lu and Y. Wang, *J. Phys. Chem. C*, 2010, **114**, 9889–9897.
2 C. F. Oliveira, F. A. C. Garcia, D. R. Araújo, J. L. Macedo, S. C. L. Dias and J. A. Dias, *Appl. Catal. A,* 2012, **413–414**, 292–300.
3 F. Ramezanipour, M. Shishkin, K. Singh, J. P. Hodges, T. Ziegler and V. Thangadurai, *J. Mater. Chem. A,* 2013, **1**, 8344–8347.
4 J. A. Rodriguez, J. C. Hanson, D. Stacchiola and S. D. Senanayake, *Phys. Chem. Chem. Phys.,* 2013, **15**, 12004–12025.
5 K. Kuntaiah, P. Sudarsanam, B. M. Reddy and A. Vinu, *RSC Adv.,* 2013, **3**, 7953–7962.
6 L. Katta, P. Sudarsanam, G. Thrimurthulu and B. M. Reddy, *Appl. Catal. B*, 2010, **101**, 101–108.
7 Y. Zhou and J. Zhou, *J. Phys. Chem. Lett.,* 2010, **1**, 1714–1720.
8 L. Katta, P. Sudarsanam, B. Mallesham and B. M. Reddy, *Catal. Sci. Technol.,* 2012, **2**, 995–1004.
9 L. Li and X. Li, *J. Phys. Chem. C*, 2013, **117**, 15383−15393.
10 D. Jampaiah, K. M. Tur, S. J. Ippolito, Y. M. Sabri, J. Tardio, S. K. Bhargava and B. M. Reddy, *RSC Adv.,* 2013, **3**, 12963−12974.
11 W. –T. Chen, K. –B. Chen, M. –F. Wang, S. –F. Weng, C. –S. Lee and M. C. Lin, *Chem. Commun.,* 2010, **46**, 3286−3288.
12 J. R. Scheffe and A. Steinfeld, *Fuels,* 2012, **26**, 1928−1936.
13 X. Yao, C. Tang, Z. Ji, Y. Dai, Y. Cao, F. Gao, L. Dong and Y. Chen, *Catal. Sci. Technol.,* 2013, **3**, 688–698.
14 M. Balaguer, C. Y. Yoo, H. J. M. Bouwmeester and J. M. Serra, *J. Mater. Chem. A*, 2013, **1**, 10234–10242.
15 B. M. Reddy, P. Bharali, P. Saikia, A. Khan, S. Loridant, M. Muhler and W. Gruenert, *J. Phys. Chem. C Lett.,* 2007, **111**, 1878–1881.
16 Q. Dong, S. Yin, C. Guo, T. Kimura and T. Sato, *RSC Adv.,* 2012, **2**, 12770–12774.
17 K. Ahn, D. S. Yoo, D. H. Prasad, H. W. Lee, Y. C. Chung and J. H. Lee, *Chem. Mater.,* 2012, **24**, 4261−4267.
18 J. Vecchietti, S. Collins, W. Xu, L. Barrio, D. Stacchiola, M. Calatayud, F. Tielens, J. J. Delgado and A. Bonivardi, *J. Phys. Chem. C,* 2013, **117**, 8822−8831.
19 M. Guo, J. Lu, Y. Wu, Y. Wang and M. Luo, *Langmuir,* 2011, **27**, 3872–3877.
20 W. Y. Hernández, M. A. Centeno, F. Romero-Sarria and J. A. Odriozola, *J. Phys. Chem. C,* 2009, **113**, 5629–5635.
21 O. H. Laguna, M. A. Centeno, M. J. Boutonnet and A. Odriozola, *Appl. Catal. B*, 2011, **106**, 621–629.
22 P. Sudarsanam, B. Mallesham, P. S. Reddy, D. Großmann, W. Grünert and B. M. Reddy, *Appl. Catal. B,* 2014, **144**, 900–908.
23 S. Sun, X. Zhao, H. Lu, Z. Zhang, J. Wei and Y. Yang, *CrystEngComm,* 2013, **15**, 1370–1376.
24 D. G. Pintos, A. Juan and B. Irigoyen, *J. Phys. Chem. C,* 2013, **117**, 18063−18073.
25 Z. Zhang, D. Han, S. Wei and Y. Zhang, *J. Catal.,* 2010, **276**, 16–23.
26 Y. Zuo, X. Huang, L. Li and G. Li, *J. Mater. Chem. A*, 2013, **1**, 374–380.
27 W. J. Hong, S. Iwamoto and M. Inoue, *Catal. Lett.*, 2010, **135**, 190–196.
28 C. Liang, Z. Ma, H. Lin, L. Ding, J. Qiu, W. Frandsen and D. Su, *J. Mater. Chem.*, 2009, **19**, 1417–1424.
29 A. Hedayati, A. M. Azad, M. Rydén, H. Leion and T. Mattisson, *Ind. Eng. Chem. Res.,* 2012, 51, 12796–12806.
30 S. Yin, Y. Minamidate, S. Tonouchi, T. Goto, Q. Dong, H. Yamanea and T. Sato, *RSC Adv.,* 2012, **2**, 5976–5982
31 F. J. Perez-Alonso, I. Melián-Cabrera, M. L. Granados, F. Kapteijn and J. L. G. Fierro, *J. Catal.,* 2006, **239**, 340–346.
32. P. Sudarsanam, B. M. Reddy, in *Nanotechnology Commercialization,* ed. T. Tsuzuki, Pan Stanford Publishing, Singapore, 2013, ch. 3, pp. 73–138.
33 P. Sudarsanam, L. Katta, G. Thrimurthulu and B. M. Reddy, *J. Ind. Eng. Chem.,* 2013, **19**, 1517–1524.
34 T. Li, G. Xiang, J. Zhuang and X. Wang, *Chem. Commun.,* 2011, **47**, 6060–6062.
35 Q. Yu, X. Wu, C. Tang, L. Qi, B. Liu, F. Gao, K. Sun, L Dong and Y. Chen, *J. Colloid Interface Sci.*, 2011, **354**, 341–352.
36 B. Mallesham, P. Sudarsanam, G. Raju and B. M. Reddy, *Green Chem.,* 2013, **15**, 478–489.
37 R. Gao, D. Zhang, P. Maitarad, L. Shi, T. Rungrotmongkol, H. Li, J. Zhang and W. Cao, *J. Phys. Chem. C,* 2013, **117**,

10502−10511.
38 H. –F. Wang, H. –Y. Li, X. –Q. Gong, Y. –L. Guo, G. –Z. Lu and P. Hu, *Phys. Chem. Chem. Phys.,* 2012, **14**, 16521–16535.
39 J. Paier, C. Penschke and J. Sauer, *Chem. Rev.,* 2013, **113**, 3949−3985.
40 W. F. Lim and K. Y. Cheong, *J. Phys. Chem. C*, 2013, **117**, 14014−14024.
41 D. Gamarra, A. L. Cámara, M. S. Monte, B. Rasmussen, L. E. Chinchilla, A. B. Hungría, G. Munuera, N. Gyorffy, Z. Schay, V. C. Corberán, J. C. Conesa and A. Martínez-Arias, *Appl. Catal. B*, 2013, **130–131**, 224–238.
42 H. Bao, X. Chen, J. Fang, Z. Jiang and W. Huang, *Catal. Lett.,* 2008, **125**, 160–167.
43 M. Giarola, G. Mariotto and D. Ajò, *J. Raman Spectrosc.,* 2012, **43**, 556–558.
44 B. M. Reddy, L. Katta and G. Thrimurthulu, *Chem. Mater.,* 2009, **22**, 467–475.
45 P. Sudarsanam, B. Mallesham, D. N. Durgasri and B. M. Reddy, *J. Ind. Eng. Chem.,* (doi:10.1016/j.jiec.2013.11.053).
46 Z. Wang, Q. Wang, Y. Liao, G. Shen, X. Gong, N. Han, H. Liu and Y. Chen, *ChemPhysChem,* 2011, **12**, 2763−2770.
47 M. A. Ebiad, D. R. Abd El-Hafiz, R. A. Elsalamony and L. S. Mohamed, *RSC Adv.,* 2012, **2**, 8145–8156.
48 A. S. Reddy, C. Y. Chen, C. C. Chen, S. H. Chien, C. J. Lin, K. H. Lin, C. L. Chen and S. C. Chang, *J. Mol. Catal. A,* 2010, **318**, 60–67.
49 K. Li, H. Wang, Y. Wei and D. Yan, *Appl. Catal. B,* 2010, **97**, 361–372.
50 S. Ma, G. Lu, Y. Shen, Y. Guo, Y. Wang and Y. Guo, *Catal. Sci. Technol.,* 2011, **1**, 669–674.